

PHYSICAL PARAMETERS OF THE TORUS FOR THE TYPE 2 SEYFERT IC 5063 FROM MID-IR AND X-RAY SIMULTANEOUS SPECTRAL FITTING

DONAJI ESPARZA-ARREDONDO,¹ OMAIRA GONZÁLEZ-MARTÍN,¹ DEBORAH DULTZIN,² CRISTINA RAMOS-ALMEIDA,^{3,4}
JACOPO FRITZ,¹ JOSEFA MASEGOSA,⁵ ALICE PASETTO,¹ MARIELA MARTÍNEZ-PAREDES,⁶ NATALIA OSORIO-CLAVIJO,¹ AND
CESAR VICTORIA-CEBALLOS¹

¹*Instituto de Radioastronomía y Astrofísica (IRyA-UNAM), 3-72 (Xangari), 8701, Morelia, Mexico*

²*Instituto de Astronomía (IA-UNAM), Mexico city, Mexico*

³*Instituto de Astrofísica de Canarias (IAC), C/Va Lctea, s/n, E-38205 LaLaguna, Spain*

⁴*Departamento de Astrofísica, Universidad de La Laguna (ULL), E-38205 La Laguna, Spain*

⁵*Instituto de Astrofísica de Andalucía (CSIC), Glorieta de la Astronomía s/n 18008, Granda, Spain*

⁶*Korea Astronomy and Space Science Institute 776, Daedeokdae-ro, Yuseong-gu, Daejeon 34055, Republic of Korea*

(Received ??; Revised ??; Accepted ??)

Submitted to ApJ

ABSTRACT

In order to understand the diversity of classes observed in active galactic nuclei (AGN), a geometrically and optically thick torus of gas and dust is required to obscure the central engine depending on the line of sight to the observer. We perform a simultaneous fitting of X-ray and mid-infrared (mid-IR) spectra to investigate if the same structure could produce both emissions and, if this the case, to obtain better constraints for the physical parameters of the torus. In this case we take advantage of the fact that both emissions show important signatures of obscuration. We used the nearby type-2 active nucleus IC 5063 as a test object. This object is ideal because of the wealth of archival data including some high resolution data. It also has a relatively high AGN luminosity that dominates at both X-ray and mid-IR frequencies. We use high spectral resolution *NuSTAR* and IRS/*Spitzer* spectra. The AGN dusty models used several physically motivated models. We found that the combination of the smooth torus models at mid-IR by Fritz et al. (2006) and at X-rays by Baloković et al. (2018), with the viewing and half-opening angles linked to the same value, is the best choice to fit the spectra at both wavelengths. This allows us to determine all the parameters of its torus. This result suggests that the structure producing the continuum emission at mid-IR and the reflection component at X-ray is the same. Therefore, we prove that this technique can be used to infer the physical properties of the torus, at least when AGN dust dominates the mid-IR emission and the reflection component is significant at X-rays.

1. INTRODUCTION

According to the simple unification model (UM) of active galactic nuclei (AGN), a toroidal structure (broadly referred as the torus) provides the anisotropic obscuration needed to explain the diversity of AGN properties observed across the electromagnetic spectrum (Antonucci 1993; Urry & Padovani 1995). The line of sight (LOS) to the observer with respect to the torus, its geometry, chemical composition, and distribution are keys to understand AGN diversity, perhaps linked to fundamental changes for different AGN classes (Shlosman 2005; Elitzur & Netzer 2016).

This torus absorbs optical/UV accretion disc radiation and re-emits it at infrared wavelengths (see Netzer 2015; Ramos-Almeida & Ricci 2017, for a review). Radiative transfer models based dust distributed on a toroidal geometry have been proven to be successful in reproducing the infrared spectral energy distribution (SED) of AGN (e.g. Hatziminaoglou et al. 2008, 2009; Ramos-Almeida et al. 2009; Alonso-Herrero et al. 2011; Hönig & Kishimoto 2017). Initially, most authors used smooth dust distributions with different radial and vertical density profiles by simplicity (e.g. Pier & Krolik 1993; Granato & Danese 1994; Efstathiou & Rowan-Robinson 1995; Schartmann et al. 2005; Fritz et al. 2006). It was later proposed that the dust is most probably arranged in clouds instead of being smoothly distributed (e.g. Krolik & Begelman 1988; Tacconi et al. 1994). The dusty torus has been the subject of several kinds of models that aimed to extract physical (e.g. optical depth) and geometrical (e.g. orientation and size) properties from SED and, in some cases, interferometric observations. We can divide them into four kinds: smooth (Fritz et al. 2006), clumpy (Nenkova et al. 2008a,b; Hönig et al. 2010a; Hönig & Kishimoto 2010b), smooth + clumpy (Stalevski et al. 2012; Siebenmorgen et al. 2015), and windy (Hönig & Kishimoto 2017). Since two decades already, adjusting models to IR spectra and broad band SEDs, has been the one and only mean in the attempt to derive clues on the dust geometry, composition and on its geometrical distribution.

Furthermore, signatures of reprocessing emission by the torus in the X-ray band arise primarily from interaction of X-ray photons with the surrounding gas (Ghisellini et al. 1994; Krolik et al. 1994). The main two features are the neutral iron line around 6.4 keV (FeK α) and the Compton hump peaking at ~ 10 -30 keV. These features have been observed in the X-ray spectra of most AGN (e.g. Matt et al. 1991; Ricci et al. 2014). Reprocessed continua are known to vary as a function of geometry of the reprocessing material (Nandra & George 1994). It has been suggested that both the Compton

hump and the narrow cores of the FeK α emission line in AGNs are likely produced in the torus (see Shu et al. 2010; Liu & Wang 2010; Fukazawa et al. 2016), being an ubiquitous component in Seyfert galaxies (Bianchi et al. 2004). Therefore, X-ray spectral fitting to the high energy continuum emission (above 10 keV) and the FeK α line might provide important information about the torus geometry, cloud distribution, and opacity.

The 100-fold increase in sensitivity in the hard X-ray band (>10 keV) brought by *NuSTAR* (Harrison et al. 2013) made possible to study the spectral signatures of the torus for the first time. Empirically, spectral models with approximately toroidal geometry have been calculated by Murphy & Yaqoob (2009) (MyTorus), Ikeda et al. (2009), Brightman & Nandra (2011) (BNtorus), Liu & Li (2015) (ctorus), Furui et al. (2016) (MONACO), and Baloković et al. (2018) (borus02). Several of them are currently available to the community.

For this work, we selected the type-2 Seyfert IC 5063 as a test object. This AGN is located at the center of a nearly lenticular galaxy at 46 Mpc (Alonso-Herrero et al. 2011). This galaxy contains a disc with large-scale dust lanes (Morganti et al. 1998), possibly resulting from a merger (Morganti et al. 1998). According to Ichikawa et al. (2015) the bolometric luminosity of IC 5063 is $3.38 \times 10^{44} \text{ erg s}^{-1}$. At X-ray wavelengths, IC 5063 has been observed with *GINGA* (Koyama et al. 1992), *ASCA* (Tanaka et al. 1994), and *ROSAT* (Pfeffermann et al. 1987; Vignali et al. 1997). More recently, IC 5063 was observed at X-ray wavelengths with *NuSTAR* (Baloković et al. 2018, see also Balokovic in prep for details on the X-ray spectral analyses). At infrared wavelengths, Peeters et al. (2004) observed this source with the ISO satellite determining that it is dominated by the AGN with little evidence of polycyclic aromatic hydrocarbon (PAHs) molecule emission. The dusty torus properties of IC 5063 have been explored through high angular resolution near and mid-IR photometric data (Ramos-Almeida et al. 2009, 2011; Alonso-Herrero et al. 2011) and clumpy models of Nenkova et al. (2008a,b), allowing a direct comparison with our results.

In this paper, we present a new technique to combine X-ray and mid-IR spectral information to make a simultaneous fit to torus models. We demonstrate that our method can successfully constrain the torus parameters and obtain information more complete in both ranges of wavelengths. The X-ray and mid-IR observations are presented in Section 2. Subsequently, the spectral fitting methodology is shown in Section 4. The main results and discussion, within the framework of our goals, are presented in Sections 5 and 6. Finally, a brief summary and conclusions are given in Section 7.

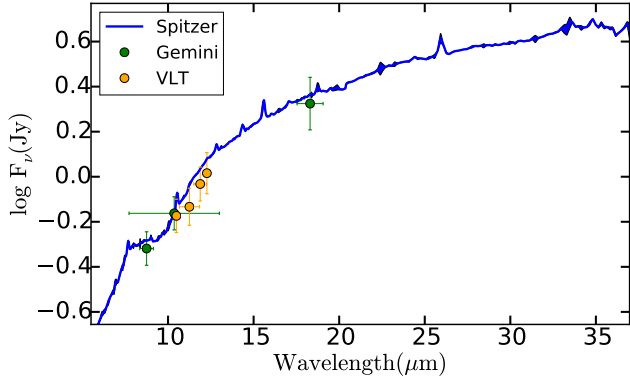


Figure 1. The *Spitzer*/IRS spectrum and photometric data. The orange and green points are measurements from VLT and Gemini, respectively.

2. DATA

2.1. X-ray data

There are several X-ray observations available in the archives of different satellites for IC 5063. However, we need to cover energies above 10 keV because it is the aim of this paper to constrain the reflection component associated to the torus. The *NuSTAR* is the first focusing hard X-ray telescope with high sensitivity¹. This gives the advantage to observe with a single mode from ~ 3 –79 keV, perfectly suited to study the AGN reflection component. Therefore, we use the hard band spectrum observed with *NuSTAR* (Harrison et al. 2013), including both FPMA and FPMB focal plane modules. *NuSTAR* has observed IC 5063 once (ObsID 60061302002, P.I. Harrison) on July 8th of 2013.

NuSTAR data reduction was done using the data analysis software *NuSTARDAS* v.1.4.4 distributed by the High Energy Astrophysics Archive Research Center (HEASARC). The calibrated, cleaned and screened event files were generated using the NUPIPELINE task (CALDB 20160502). A circular region of 1 arcmin radius was taken to extract the source and background spectrum on the same detector and to compute the response files (RMF and ARF files) using the NUPRODUCTS package within *NuSTARDAS*. Finally, we used the GRPPHA task within the FTOOLS to group the spectra with at least 60 counts per bin. The net exposure is 18.4 ksec. We found some cross-calibration issues between the FPMA and FPMB modules, larger below ~ 3 keV. We used the *NuSTAR* data above 3 keV to avoid them.

2.2. Mid-IR data

Regarding the IR data, we used the high-resolution *Spitzer*/IRS spectrum downloaded from the CASSIS² catalog (the Cornell Atlas of *Spitzer*/IRS Sources, Lebouteiller et al. 2011). The spectral resolution of *Spitzer*/IRS ($R \sim 60 - 130$) is similar to that obtained by ground based observations. The *Spitzer*/IRS spectrum could have a high contribution of galaxy emission due to its relative low spatial resolution. Note that we could overcome this issue by including stellar libraries to the fit. However, the inclusion of these libraries significantly worsen the estimate of the resulting parameters (González-Martín et al. 2019a,b). In order to investigate it, we compared this spectrum with ground-based high spatial resolution fluxes (see Figure 1). In particular, we compiled VISIR/VLT and T-ReCS/Gemini fluxes in Si2_{8.73μm}, N-band_{10.4μm}, SIV_{10.5μm}, PAH2_{11.3μm}, NEII_{11.2.3μm}, and Qa_{18.2μm} filters reported in NED³ (Hönig et al. 2010a; Ramos-Almeida et al. 2011). These data provide high-spatial resolution fluxes (~ 100 pc). We found that the *Spitzer*/IRS spectrum shows slightly higher fluxes than the VLT and Gemini photometric data points, although those are well in agreement when ground-based flux calibration uncertainties are taken into account (15% at N-band and 25% at Q-band of the flux according e.g. Ramos-Almeida et al. 2011).

In fact, Asmus et al. (2014) studied the T-ReCS and VISIR images of IC 5063 and found a compact but consistently elongated mid-IR nucleus (FWHM(major axis) ~ 0.52 arcsec ~ 110 pc; PA $\sim 107^\circ$) without any further host emission detected. They found that the direction of this elongation coincides with the extended [O III] line emission. Additionally, Hönig et al. (2010a) compares the photometric data with the *Spitzer*/IRS and VISIR spectra extracted over 0.75 arcsec and found that the that agrees well. Indeed, according to Panuzzo et al. (2011) the continuum of IC 5063 in the low resolution *Spitzer*/IRS spectrum is dominated by hot dust, most probably coming from the AGN torus. They did not find PAH feature emission, although some forbidden lines were detected. The lack of strong stellar or starburst components makes the *Spitzer*/IRS spectrum of IC 5063 ideal to study the torus parameters throughout mid-IR spectral fitting.

In order to perform spectral fitting to the data, we converted the mid-IR *Spitzer*/IRS spectrum into XSPEC format using FLX2XSP task within HEASOFT. This tool reads a text file containing one or more spec-

¹ <https://heasarc.gsfc.nasa.gov/docs/nustar/>

² <http://cassis.astro.cornell.edu/atlas/>

³ <https://ned.ipac.caltech.edu/>

tra and errors and writes out a standard XSPEC pulse height amplitude (PHA⁴) file and response file. This will allow us to perform X-ray and mid-IR simultaneous fit too.

3. THE MID-IR AND X-RAY MODELS

We give here a brief summary on the characteristics of the models used to fit X-ray and mid-IR spectra. Both wavelengths carry information on the torus-like structure that obscures the accretion disc for certain viewing angles. Both models are produced using radiative transfer codes including the physics required to account for mid-infrared and X-ray main continuum features. The mid-IR models include re-emission due to dust while X-ray models mainly include reflection in neutral gas.

3.1. X-ray model

The bulk of the AGN emission is produced in the accretion disc and emitted at optical and ultraviolet (UV) wavelengths. A portion of this emission is reprocessed by a corona of a hot electrons plasma close to the accretion disc that scatters the energy in the X-ray bands due to inverse Compton (Netzer 2015; Ramos-Almeida & Ricci 2017, and references therein). This comptonization produces one of the three main components of X-ray spectra known as the intrinsic continuum. It is modelled by a power law with a spectral index (Γ) typically around 1.8-2.3 (e.g. Yang et al. 2015). This feature dominates the spectral emission above 2 keV and it is a distinctive signature of the AGN emission. Some part of this primary emission is absorbed by the torus or the broad line region and another is reprocessed by a distant material (e.g. the inner walls of the torus) and it gives place to the second most relevant component, named Compton hump with a maximum of its emission at ~ 30 keV (Ricci et al. 2011). The reflection component depends on the shape of the reprocessing material, both its geometry and density (Ghisellini et al. 1994). This structure could be the torus and depends mainly on the geometrical covering factor of the reprocessed material and its average N_H . The third component is the FeK α emission line, which origin is the reflection of X-ray photons. The origin of the narrow FeK α line might also be associated to the torus, while the broad FeK α line is thought to be originated in the inner parts of the accretion disc (Fabian 1998; Laor 1991). This analysis is based on the hypothesis that the reprocessor is the torus, which seems to be the case for the vast majority of the sources (Matt et al. 1991).

The reflection component of AGN has been studied through different models (e.g. Murphy & Yaqoob 2009; Ikeda et al. 2009; Brightman & Nandra 2011; Liu & Li 2015). In this work, we used a new grid of X-ray spectral templates called borus02 model presented by Baloković et al. (2018). These templates were based on BORUS, a radiative transfer code which assumes a toroidal geometry of neutral gas. To generate the borus02 templates the geometry was simplified as a smoother toroidal distribution of gas. This geometry approximation is represented as a uniform-density sphere with two conical polar cutouts with the opening angle as a free parameter, such as the one employed by Brightman & Nandra (2011) (see also Baloković et al. 2018, for more details).

The borus02 model allows us to explore the following parameters of the torus: 1) the average column density ($N_{H_{tor}}$), 2) the relative abundance of iron ($A_{FeK\alpha}$), and 3) the angular size (θ_{tor}). Additionally, borus02 considered the incident emission in the torus as a power law with index Γ multiplied by an exponential cutoff ($e^{(-E/E_{cut})}$). Finally an additional parameter controls the viewing angle of the torus relative to the observer (θ_{inc}). Fig. 2 (top-right corner with orange labels) shows the geometry and parameters associated to borus02.

3.2. Mid-IR model

The dusty torus has been the subject of several AGN models at mid-IR wavelengths that aimed to extract physical properties from SED. In this work, we used three of these SED grids to fit our mid-IR spectra: Smooth (Fritz et al. 2006; Feltre et al. 2012), Clumpy (Nenkova et al. 2008a,b), and CAT3D-WIND (Hönig & Kishimoto 2017). These models are based on radiative transfer codes that use different geometrical distributions and compositions of dust. In Figure 2, we show a cartoon that summarises the geometry assumed for these models. Below we give a short description for each model.

- Smooth model: This model has a torus-like morphology. It was created by modelling a flared disc created as two concentric spheres, delimiting, respectively, the inner (R_{in}) and the outer (R_{out}) radius of the torus with the polar cones removed. It considers graphite grains with radius $a_G = 0.05 \mu m$ and sublimation dust temperature of 1500k to compute the R_{in} (see Eq.5 from Barvainis 1987). It describes the dust density in polar coordinates (see Eq.3 in Fritz et al. 2006) and allows to explore the following parameters of the torus: 1) the viewing angle of observer toward the torus (i_{F06}), 2) the half opening angle (σ), 3) the exponent of the logarithmic elevation density distribution (γ), 4) the exponent of the power law of the radial profile of the density dis-

⁴ Engineering unit describing the integrated charge per pixel from an event recorded in a detector.

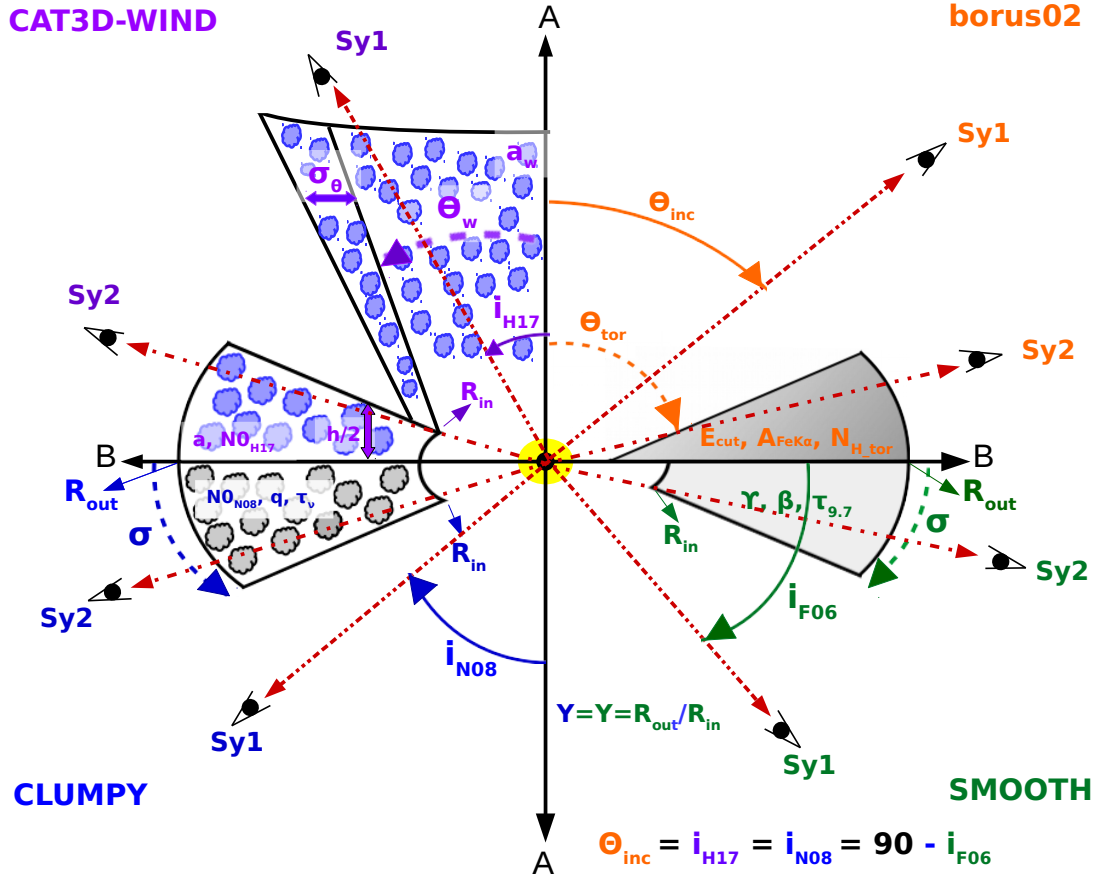


Figure 2. Geometry of the borus02 and the three mid-IR models used in this paper. The borus02 model by Baloković et al. (2018) is shown as a torus cut surface above the equatorial plane and filled in dark gray gradient. The smooth torus model by Fritz et al. (2006) is shown as a torus cut surface below the equatorial plane and filled in light gray. The clumpy torus model by Nenkova et al. (2008b) is shown as a torus cut surface below the equatorial plane filled with gray clouds. Clouds represent models with clumpy distribution of dust. The parameters for each model are shown with different colors: borus02 (orange), Smooth (green), Clumpy (blue), CAT3D-WIND (purple), and borus02 (orange). In all of them we show an example of a view for a Sy1 and a Sy2.

tribution (β), 5) the equatorial optical depth at $9.7 \mu\text{m}$ ($\tau_{9.7 \mu\text{m}}$), and 6) the outer-to-inner radius ratio (Y).

- **Clumpy model:** The clumpy model considers a formalism where an AGN is surrounded by a toroidal distribution of dusty clouds. This assumes a standard Galactic composition (of 53% silicates and 47% graphite) of dust. Among them the most extensively used one is the Clumpy model of Nenkova et al. (2008b) (although see also Hönig & Kishimoto 2010b) due to their large number of SEDs and probed ability to explain the mid-IR emission of low luminous (González-Martín et al. 2017), intermediate luminous (e.g. Ramos-Almeida et al. 2009), and high luminous (Martínez-Paredes et al. 2017) AGNs. The model parameters are: 1) the viewing

angle (i_{N08}) respect to the polar plane, 2) the number of clouds in the equatorial plane of the torus (N_{0N08}), 3) the half angular width of the torus (σ), 4) the ratio between the inner and the outer radius ($Y = R_{\text{out}}/R_{\text{in}}$), 5) the slope of the radial distribution of clouds described by a power law (q), and the optical depth for the individual clouds (τ_ν).

- **CAT3D-WIND model:** The CAT3D-WIND model is built upon the hypothesis that the dust around the AGN consists of a geometrically thin disc of optically thick dust clumps and a outflowing wind described by a hollow cone composed by dusty clouds. The near-IR emission up to $\sim 5 \mu\text{m}$ is due to an inflowing disc in the equatorial plane, while the main contributor to mid-IR

emission is the polar dust. The distribution of the dust clouds in the disc is described with the following parameters: 1) the power law slope (a), 2) the inner radius (R_{in}) that denotes the distance from the AGN in units of the sublimation radius, 3) the dimensionless scale height (h) from the mid-plane of the disc of the vertical Gaussian distribution of clouds in units of the sublimation radius, and 4) the average number of dust clouds (N_{0H17}) along the equatorial LOS of the disc. The polar outflow is modeled as a hollow cone with the following parameters: 1) the radial distribution of dust clouds in the wind (a_w), 2) the half-opening angle of the wind (θ_w), and 3) the angular width (σ_θ). Finally, two further parameters are common to both components, such as the inclination angle towards the observer (i_{H17}) and the ratio between the number of clouds along the cone and N_{0H17} of the disc (fwd). This model considers a standard composition disc (similar to clumpy models) and an outflow composed by large grains.

The SEDs produced by the smooth and the clumpy models are defined in a $0.001 \mu\text{m}$ - $1000 \mu\text{m}$ wavelength range and those produced by the CAT3D-WIND model cover a wavelength range between $0.01 \mu\text{m}$ and $36,000 \mu\text{m}$.

3.3. Derived quantities

3.3.1. Covering factor

We calculate Cf in both X-ray and mid-IR models. We use the relationship between the Cf and θ_{tor} given by: $Cf = \cos(\theta_{tor})$. Note that this is a simplistic approximation that assumes that the clouds take up most of the torus volume, following the prescription given by Baloković et al. (2018).

We can also calculate the Cf using the mid-IR parameters. To derive the equation of the Cf of Smooth model (Cf_{F06}), we take into account the extinction coefficient, the density distribution along the radial and polar distances, the normalization constant, and β value (see equation 3 from Fritz et al. 2006). Note that we assumed a $\beta = 0$ because this number only have two values in the SED provided (0 or 1) and we obtained a value close to zero for our best fit. For the Clumpy model we calculate this Cf (Cf_{N08}) using the equation 9 from (Nenkova et al. 2008a) and the angular distribution of clumps (Feltre et al. 2012). A similar equation is used to calculate the Cf for each component (wind and disc) for the CAT3D-wind model, with the total Cf as the sum of the two components. Note that the Cf of the wind, is calculated as the subtraction of two toroidal structures as in Hönig et al. (2010a) with a half opening angle of $\theta_w + \sigma_\theta$ and θ_w , respectively. Using our nota-

tion for each parameter, these are the equations required to compute Cf :

- Smooth model (case $\beta = 0$)

$$Cf_{F06} = \frac{\ln(\tau_{9.7})}{\gamma} \quad (1)$$

- Clumpy model

$$Cf_{N08} = 1 - \int_0^{\pi/2} \cos\beta e^{N_{0N08} e^{-\beta^2/\sigma^2}} d\beta \quad (2)$$

- CAT3D wind model

$$Cf_{H17} = 1 + \int_0^{\pi/2} \cos\theta e^{N_{0w} e^{-\theta^2/\theta_w^2}} d\theta - \int_0^{\pi/2} \cos\theta e^{N_{0w} e^{-\theta^2/(\theta_w + \sigma_\theta)^2}} d\theta - \int_0^{\pi/2} \cos\theta e^{N_{0d} e^{-\theta^2/\sigma_d^2}} d\theta \quad (3)$$

where $\sigma_d = \arctan h/2$.

3.3.2. Dust Mass

We also estimate the total dust mass (M_{tor}) using the parameters obtained for each model. This value is obtained from the integration of the density distribution of dust over the volume. We use the equation 9 from Mor et al. (2009) given $q = 2$ for the Clumpy model. We follow the equations in table 1 from Hönig et al. (2010a) to compute the mass for the CAT3D disc-wind model. We sum up the contributions of the disc and the wind, with the latter obtained as the subtraction of two toroidal distribution with angular width of $\theta_w - \sigma_\theta$ and θ_w . Note that we analytically derive the mass equations assuming $\beta = 0$ for the Smooth model and $q = 2$ for the Clumpy model because these values are close to the results that we find for our object (see Table 1 and Section 5). Using our notation for each parameter, the equations to compute the total dust mass are:

- Smooth model ($\beta = 0$)

$$M_{tor}(F06) = \frac{4\pi\tau_{9.7}}{3\kappa\gamma} \frac{(R_{out}^3 - R_{in}^3)(1 - e^{-\gamma})}{R_{out} - R_{in}} \quad (4)$$

where κ is extinction coefficient in the Milky Way.

- Clumpy model ($q = 2$)

$$M_{tor}(N_{0N08}) = 4\pi \sin(\sigma) N_{0N08} * N R_{in}^2 Y \frac{Y}{2 \log_{10} Y} \quad (5)$$

where $N = N_H * A_\nu * mH$ is the N_H multiplied by the extinction due to dust (obtained from τ_ν and assuming a constant dust-to-gas ratio) times the hydrogen mass in units of kg for a single cloud.

- CAT3D-wind model⁵

$$M_{tor}(H17) = \frac{N\sqrt{\pi}}{R_{cl;0}^2} \quad (6)$$

$$\times (N_{0w}(f_{\theta_w - \sigma_\theta} - f_{\theta_w}) + N_{0d}f_{\sigma_d})$$

where f_{θ_0} function is defined as (Hönig et al. 2010a)

$$f_{\theta_0} = \theta_0 e^{-\theta_0^2/4} \quad (7)$$

$$\times \left(\text{Erf} \frac{\pi - i\theta_0^2}{2\theta_0} + \text{Erf} \frac{\pi + i\theta_0^2}{2\theta_0} \right)$$

The constant dust-to-gas ratio relation assumed is $N_H = 1.9 \times 10^{21} * 1.086 * \tau_\nu$ (Bohlin et al. 1978).

4. SPECTRAL FITTING

Spectral fitting is performed using the XSPEC fitting package. XSPEC is a command-driven, interactive, spectral-fitting tool within the HEASOFT⁶ software. XSPEC has been used to analyze X-ray data such as *ROSAT*, *ASCA*, *Chandra*, *XMM-Newton*, *Suzaku*, *NuSTAR*, or *Hitomi*. XSPEC allows users to fit data with models constructed from single emission components coming from different mechanisms and/or physical regions. XSPEC already includes a large number of models but new ones can be incorporated using the ATABLE task. The borus02 templates have been included in XSPEC using this tool. In particular we use the χ^2 statistics (through the standard $\chi_r^2 = \chi^2/\text{d.o.f.}$, where d.o.f is the number of degrees of freedom which is equal to the number of data bins in the spectrum minus the number of free parameters) and we assess the goodness-of-fit performing a test to reject the null hypothesis that the observed data are drawn from the model. The parameter confidence regions are found by surfaces of constant delta statistic from the best-fit value (ERROR task). Finally, XSPEC also allows us to find simultaneous confidence regions of multiple parameters to study the degeneracy among parameters.

X-ray data and models used in this analysis are already formatted to be used within XSPEC. To use these capabilities for the mid-IR spectra (and simultaneous X-ray and mid-IR fitting), we converted the data (see Section 2) and models (see Section 4.1 below) to XSPEC format.

4.1. Mid-IR models in XSPEC

⁵ Note that these equations are derived from Hönig et al. (2010a) assuming $b = 1$ as in Hönig & Kishimoto (2017).

⁶ <https://heasarc.gsfc.nasa.gov>

We converted the mid-IR models SED libraries to multi-parametric models within the spectral fitting tool XSPEC as an additive table. The basic concept of a table model in XSPEC format is that the file contains a N-dimensional grid of model spectra with each point on the grid calculated for particular values of the N parameters in the model. XSPEC will interpolate on the grid to get the spectrum for the parameter values required at that point in the fit. To adapt mid-IR models we firstly created a one-parameter table (in fits format) associated to all the SEDs using the FLX2TAB task within HEASOFT. Note that each of the SEDs have been interpolated using 5,000 steps between the minimum and maximum wavelengths due to the need of equally spaced SEDs. We then, wrote a python routine to change the headers associating each SED to a set of parameters. This model has the free parameters described in Section 3.2 plus redshift and normalization. For the clumpy model we were not able to obtain a XSPEC model using the entire SED library due to the unpractical size of the final model (over 100 GB). Instead of $N_0 = [1-15]$ and $\sigma = [15-70]$ in steps of 1 and 5, respectively, we slightly constrained the number of clouds and the angular width of the torus to the ranges $N_0 = [1,3,5,7,9,11,13,15]$ and $\sigma = [15,25,35,45,55,65,70]$, respectively. This is in order to recover a more transferable model (~ 6 GB). Note that this does not affect our results since XSPEC interpolates between models to find the best solution.

4.2. The total model in XSPEC

We fit the mid-IR and X-ray spectra of IC 5063 following a command sequence in XSPEC:

$$\begin{aligned} & phabs * (atable\{borus02\} + zdust * zphabs * cabs * cutoffpl) \\ & + zdust * atable\{midIR_{model}\} \end{aligned} \quad (8)$$

where *phabs* is the foreground galactic absorption⁷. The model borus02⁸ accounts for the reflection component. The *zdust * zphabs * cabs* represents the line-of-sight absorption at the redshift of the source. Following the recipe provided by Baloković et al. (2018), we linked the N_H component to the *zphabs* to take into account for the total extinction along the line-of-sight, including the Compton scattering losses. We realised that these X-ray absorbers are not evaluated at energies below 10^{-4} keV. Therefore, mid-IR and X-ray simultaneous fit requires that the X-ray intrinsic emission is properly absorbed below those energies. For that reason we introduced a

⁷ In the case of IC 5063 this value is fix to $0.067 \times 10^{22} \text{ cm}^{-2}$, obtained by the NH tool within Heasoft.

⁸ We used the *borus02.v170323c.fits* file from <http://www.astro.caltech.edu/~mislavb/download/>

zdust component to neglect any artificial contribution of this component to mid-IR wavelengths. This model is also used to incorporate foreground extinction at mid-IR wavelengths. We fixed the E_{cut} parameter to 300.0 keV because our X-ray spectra only cover a wavelength range between 3-100 keV. Also, we fixed the $A_{\text{FeK}\alpha}$ parameters to the solar value. We varied these parameters on the final fit but they did not produce any statistical improvement. Finally, the *midIR_{model}* is one of the three mid-IR models described in section 3.2.

Note that the main advantage of the borus02 templates for our analysis is that it allows to constrain several parameters closely linked to the mid-IR models (see following sections).

5. FITTING RESULTS

5.1. Linking viewing angles

We firstly consider that the only parameter linked between mid-IR and X-ray models is the viewing angle. Therefore, we linked to the same value the mid-IR and X-ray viewing angles as shown in Fig. 2 (i.e. $i_{F06} = 90 - \theta_{\text{inc}}$, $i_{N08} = \theta_{\text{inc}}$, and $i_{H17} = \theta_{\text{inc}}$). Table 1 shows the resulting values for each parameter after fitting simultaneously the *NuSTAR* spectra using the borus02 model and the *Spitzer*/IRS spectrum with each of the three mid-IR models (smooth torus, clumpy torus, or clumpy wind-disc models at columns 2, 3, and 4, respectively). Hereafter, we refer to these combinations of the borus02 model with either the Smooth, Clumpy, or CAT3D-wind model as bS1, bC1, and bW1 baseline models, respectively.

Regarding the X-ray parameters, we found that: (1) the $\log N_{\text{H}_{\text{tor}}}$ is independent from the mid-IR model selected; (2) the Γ shows slight changes depending on the model; and (3) the θ_{tor} and θ_{inc} strongly depend on the mid-IR model used. Note that the viewing angle θ_{inc} is constrained when using the bS1 and bW1 baseline models, and both angles are consistent with a Sy2.

The bS1 baseline model has four free mid-IR parameters; two being constrained, other two (γ and $\tau_{9.7}$) are close to the upper limit defined by the model; and β is set to $\beta = 0$, giving better results than $\beta = 1$. Only Y is close to the upper limit among the five free parameters for bC1 baseline model, being the other free parameters well constrained. Finally, among the seven free parameter of the bW1 baseline model, five are upper limits and two are lower limits.

While a direct comparison between mid-IR parameters from each model is indeed challenging, we compare some mid-IR parameters among the bS1, bC1, or/and bW1 baseline models, such as the σ , Y , $N_{0_{\text{N08}}}$ (N_{0_w}) and the power law indices of the dust radial distribu-

tions (q , γ or aw). In particular, we can compare the bC1 and the bS1 baseline model in terms of σ and Y parameters. Similar results are obtained for σ with both models. The bC1 baseline model shows a large value for the Y parameter that implies⁹ a torus size > 24 pc, compared to ~ 3.4 pc for the bS1 baseline model. The latter is in better agreement with more recent works (see references in Ramos-Almeida & Ricci 2017). We also computed the number of clouds along the wind using fwd and N_{0_d} parameters ($N_{0_w} = fwd * N_{0_d}$) for the bW1 baseline model. This number is larger than the number of clouds in the equatorial LOS for the torus obtained for the bC1 baseline model (i.e. $N_{0_{\text{N08}}}$). We found that a_w (bW1) is very similar to q (bC1), while γ has a higher value.

We used the reduced χ^2 statistic value to assess the goodness-of-fit for each model. The $\chi^2/\text{d.o.f.}$ for the bS1, bC1, and bW1 baseline models are reported in table 1. Note that there are not large differences between $\chi^2/\text{d.o.f.}$ from these three baseline models, although the bW1 baseline model shows a larger $\chi^2/\text{d.o.f.}$ than the other two baseline models and a slightly better $\chi^2/\text{d.o.f.}$ is obtained with the combination of the borus02 and smooth models (bS1 baseline model). In Figure 3, we show the IC 5063 spectra and the resulting fit using bS1 baseline model. Note that the bS1 baseline model better reproduces the [7-10] μm wavelength range compared with bC1 and bW1 baseline models (Figures 4 and 5).

We also explored the cases in which the direction of the inclination angle for the mid-IR models can be inversely related to the inclination angle for the X-ray band (i.e. $i_{F06} = \theta_{\text{inc}}$, $i_{N08} = 90 - \theta_{\text{inc}}$, and $i_{H17} = 90 - \theta_{\text{inc}}$). This scenario will represent a reflector neutral gas that fills up the gaps where the mid-IR emitting dust is not present. We also obtained the statistic values for these cases and we compared them with those obtained above (i.e. direct link between viewing angles reported in table 1). We found that this interpretation of the viewing angle is worse than that assumed before for the bS and bC1 baseline models, obtaining a $\chi^2/\text{d.o.f.}$ of 685/647 and 754/648 (i.e. $\Delta\chi^2/\text{d.o.f.}$ 4 and 6 compared to those reported in the table), respectively. Interestingly, in the case of the bW1 baseline model, we found that this new link between viewing angles is an improvement with $\chi^2/\text{d.o.f.}$ of 718/645 (i.e. $\Delta\chi^2/\text{d.o.f.} = -12$).

We reported the covering factors Cfs obtained from X-ray models using bS1, bC1, and bW1 baseline models in table 1 (quoted as Cf_{Xray}). Both bS1 and bC1 base-

⁹ Note that the inner radius of both models is set to the same value.

	bS1 baseline model	bC1 baseline model	bW1 baseline model	bS2 baseline model
	borus02 + Smooth	borus02 + Clumpy	borus02 + CAT3D-WIND	borus02 + Smooth
Parameter	$i_{F06} = 90. - \theta_{inc}$	$i_{N08} = \theta_{inc}$	$i_{H17} = \theta_{inc}$	$i_{F06} = 90. - \theta_{inc}$
(1)	(2)	(3)	(4)	(5)
Γ	$1.72 \pm_{0.06}^{0.07}$	$1.74 \pm_{0.07}^{0.06}$	$1.70 \pm_{0.08}^{0.06}$	$1.72 \pm_{0.07}^{0.07}$
$\log(N_{H_{tor}})$	$24.00 \pm_{0.06}^{0.07}$	$23.98 \pm_{0.07}^{0.02}$	$23.90 \pm_{0.08}^{0.11}$	$23.99 \pm_{0.07}^{0.08}$
$\log(N_{H_{los}})$	$23.25 \pm_{0.02}^{0.02}$	$23.25 \pm_{0.03}^{0.01}$	$23.26 \pm_{0.03}^{0.03}$	$23.25 \pm_{0.02}^{0.03}$
θ_{tor}	$60.0 \pm_{4.5}^{2.6}$	$78.3 \pm_{12.4}^{0.4}$	< 21.9	$56.0 (90. - \sigma)$
θ_{inc}	$75.4 \pm_{1.6}^{1.3}$	87.1^*	$30.80 \pm_{0.34}^{0.30}$	$75.3 \pm_{1.5}^{1.5}$
σ	$34.1 \pm_{1.9}^{0.8}$	$34.9 \pm_{14.6}^{0.2}$	-	$34.0 \pm_{1.0}^{2.7}$
Y	$14.1 \pm_{0.2}^{0.2}$	> 95.6	-	$14.1 \pm_{0.2}^{0.2}$
$\tau_{9.7}$	> 9.27	-	-	> 9.1
τ_{ν}	-	$49.3 \pm_{3.8}^{0.7}$	50.0^*	-
β	0.0	-	1.0^*	0.0
N_{0N08} or N_{0w}	-	$3.67 \pm_{0.20}^{0.03}$	> 7.46	-
σ_{θ}	-	-	< 7.2	-
θ_w	-	-	> 44.6	-
γ, q or aw	> 5.7	$2.13 \pm_{0.02}^{0.03}$	< -2.5	> 5.6
N_{0d}	-	-	> 9.97	-
a	-	-	> -0.5	-
h	-	-	> 0.5	-
fwd	-	-	> 0.72	-
$\chi^2/\text{d.o.f.}$	681/647	708/647	730/645	682/648
Derived parameters				
R_{in} (pc)	0.23*	0.23*	0.16*	0.23*
R_{out} (pc)	3.40 ± 0.05	> 23.9	450*	3.4 ± 0.05
Cf_{Xray}	$0.50 \pm_{0.07}^{0.04}$	$0.20 \pm_{0.01}^{0.21}$	< 0.92	$0.56 \pm_{0.07}^{0.04}$
Cf_{midIR}	> 0.4	0.66 ± 0.01	> 0.4	> 0.4
M_{tor} ($\times 10^5 M_{\odot}$)	> 0.06	> 30.3	$< 0.2^{**}$	> 0.06

Table 1. The best-fit physical parameters of the torus models for IC 5063. The columns 2, 3, and 4 show the resulting parameters from fits assuming that inclination angles from mid-IR and X-ray models are linked. In column 5 shows the resulting parameters from fit assuming that inclination and half opening angles from smooth and borus02 models are linked. The values marked with * are fixed parameters. **Total mass calculated as the sum of wind and disc masses ($0.03 \times 10^5 M_{\odot}$ from wind and $0.16 \times 10^5 M_{\odot}$ from disc). Note that the Cf_{X-ray} is calculated as $\cos(\theta_{tor})$, while the Cf_{midIR} depends on several parameters according with the mid-IR model chosen (see Section 3.3.1).

line models give consistent Cfs within error bars while the bW1 baseline model gives a higher Cf . Table 1 also reports the Cfs obtained using the mid-IR parameters (denoted as Cf_{midIR}). Cf for different baseline models are consistent with each other. A comparison among Cf_{Xray} and Cf_{midIR} shows compatible results for the bS and the bW1 baseline models. However, the Cf obtained from X-rays is larger than that obtained from mid-IR for the bC baseline model.

Finally, we check for the degeneracy among parameters of the fit. For this purpose we used the best fit baseline model obtained (i.e. bS). Figure 6 shows the two-dimensional χ^2 distribution for each free parameter (dotted lines). We found that most parameters are well constrained within the 3σ contours. The most contro-

versial parameter is θ_{tor} which we cannot yet restrict, being in the range [10-70] at the 2σ level. However, note that σ parameter from the Smooth model is constrained and both parameters (σ and θ_{tor}) could be directly linked (see below).

5.2. Linking both viewing and half opening angles

We test here if we can link both the viewing angle and the half opening angle in the bS1 baseline model. Conforming to the definitions of the opening angles in the smooth and the borus02 models, the link between both parameters is $\theta_{tor} = 90 - \sigma$. Hereafter, we refer to this new combination as bS2 baseline model. In column 5 from Table 1 we report the values obtained for bS2 baseline model.

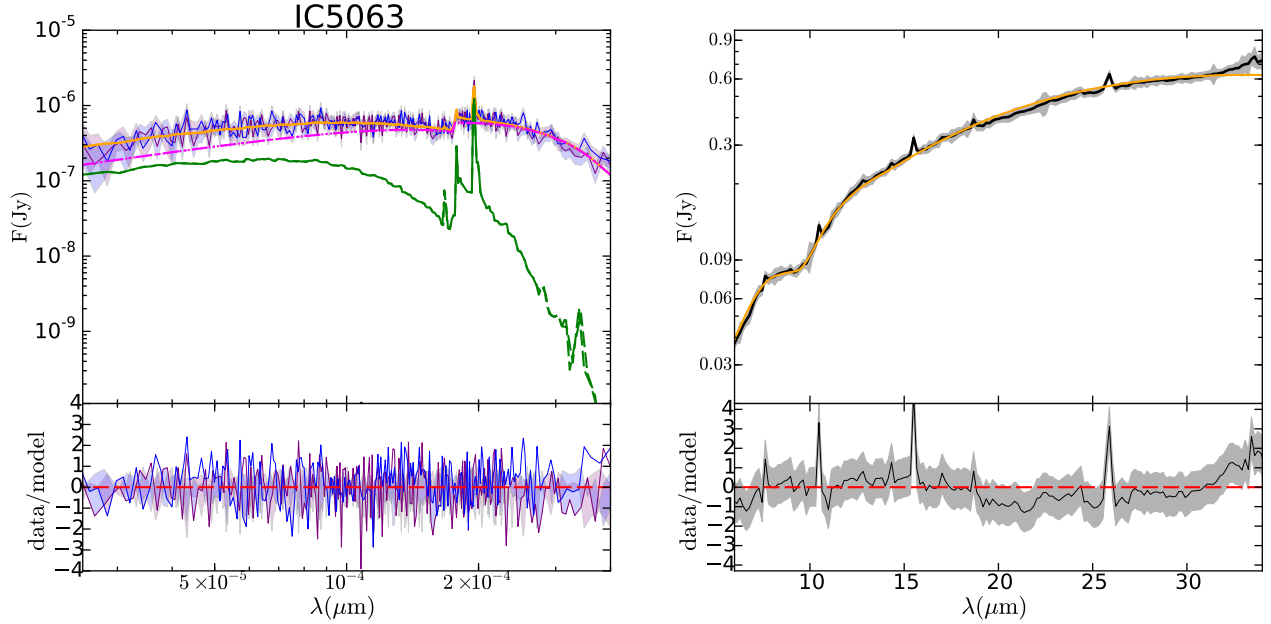


Figure 3. Unfolded spectra of IC 5063. The orange solid lines are the best-fit obtained from the bS1 baseline model. Left: *NuSTAR* spectra are displayed with blue and purple solid lines. The magenta and green dotted lines show the the absorbed power-law and the reprocessed components, respectively. Right: The *Spitzer*/IRS spectrum is shown with a black solid line. The lower panels display the residuals between data and the best-fit model.

These new parameters are consistent within the errors to those measured for the bS1 baseline model (reported in Table 1). This is the case even for σ and θ_{tor} . Note that the derived parameters Cf (X-ray), Cf (mid-IR), and M_{tor} also remain the same compared to bS1 baseline model. We compared $\chi^2/d.o.f.$ from bS and bS2 baseline models through the f-test, obtaining a probability 0.37 which is greater than 10^{-4} . Therefore, we discard the hypothesis that a most complex baseline model (bS) is better to fit the spectra; i.e., the simpler baseline model (bS2) is enough to reproduce the data.

We also check the degeneracy among the parameters for bS2 baseline model. In Figure 6, we show the two-dimensional χ^2 distribution for each combination of parameters when use the bS2 baseline model (solid lines). Note that all parameters are constrained within the 3σ contours. The advantage of linking them is that now the half opening angle is constrained for both fits. This slightly improves the calculus of the degeneracy of the parameters, showing smoother contours in Fig. 6 with no significant spoilage of the parameter restriction.

Other parameters that can be associated are $\log(N_{H_{tor}})$ and τ_ν because both are associated to the density of the medium. However, the relationship between both parameters is not simple. We explore this possibility in the next section.

6. DISCUSSION

In this work, we investigate the properties of the dusty torus of IC 5063, exploring the combination of mid-IR and X-ray spectral fits. We discuss here if the same structure producing the mid-IR continuum can also describe the reprocessed emission at X-ray wavelengths (Section 6.1), what are the resulting torus properties (Section 6.2), and if the combination can better constrain the physical parameters of the dusty structure when they are used to fit simultaneous the *Spitzer*/IRS and *NuSTAR* spectra (Section 6.3).

6.1. Link between mid-IR continuum and reprocessed emission at X-ray wavelengths

Our first step to combine the information at both wavelength ranges was to assume that the viewing angle of the torus is the same. For the bS1 and the bC1 baseline models, we found that the best options to link the mid-IR and X-ray viewing angles are $i_{F06} = 90. - \theta_{inc}$ and $i_{N08} = \theta_{inc}$, respectively. These options imply a scenario where dust and gas are in the same location (distributed along the equatorial plane). In the case of bW1 baseline model, we found that the best option is $i_{H17} = 90. - \theta_{inc}$. This scenario implies that most of mid-IR emission is in the equatorial plane. Therefore, these three baseline models are consistent with the idea that most of the dust producing the mid-IR continuum emission is distributed in the equatorial plane where the torus has historically been located. Furthermore, the X-

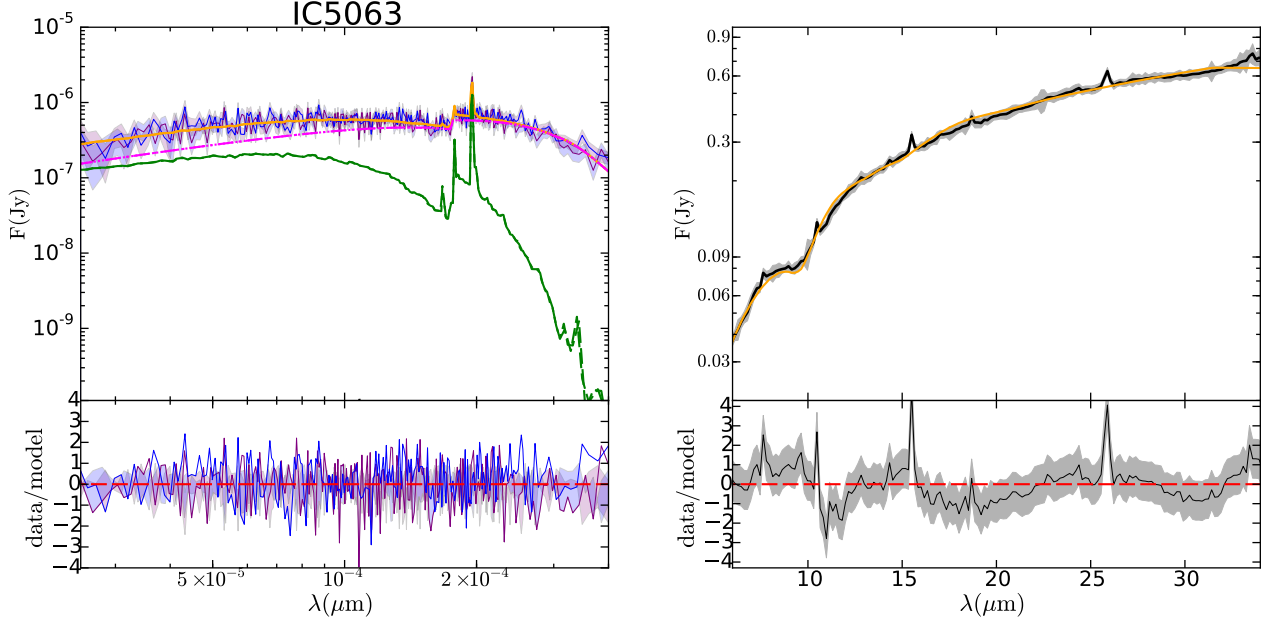


Figure 4. Same as Figure 3 but using the bN1 baseline model.

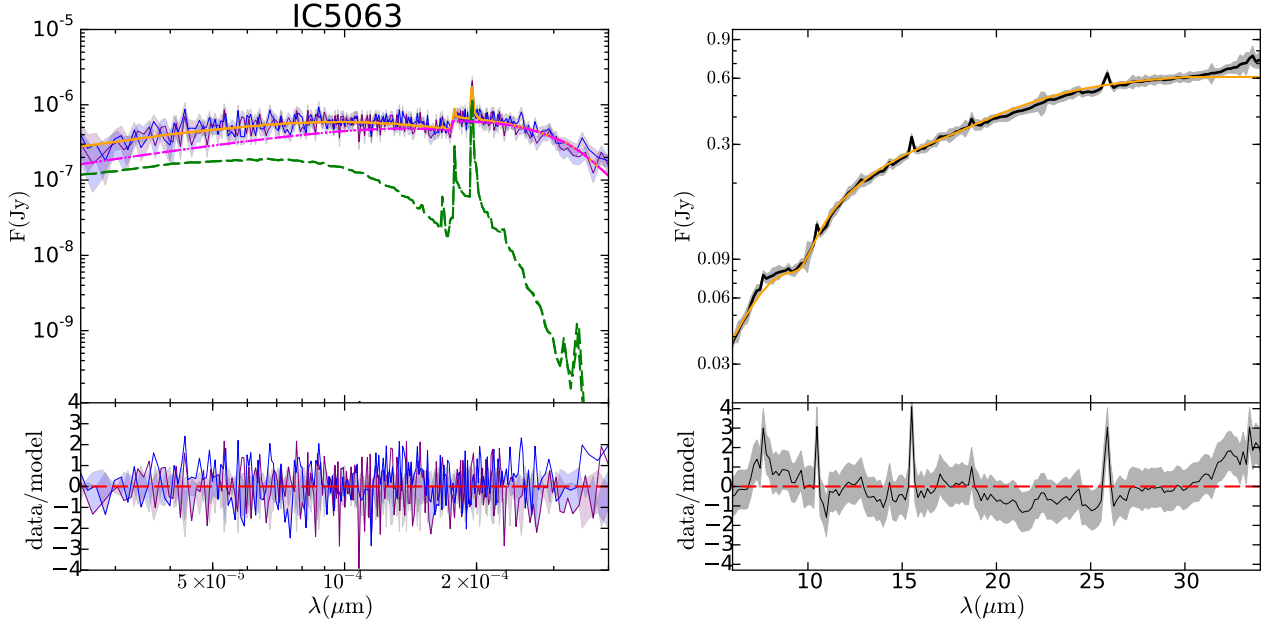


Figure 5. Same as Figure 3 but using the bW1 baseline model.

ray reflector under this scenario is also in the equatorial plane.

We reviewed and compared the reduced χ^2 statistic values for each of the baseline models. From this analysis, we concluded that the best statistic is obtained when using the combination of borus02 (X-ray) and Smooth (mid-IR) models (the so-called bS1 baseline model) to fit the spectra at both wavelengths. Even though this baseline model has the best reduced χ^2 it is not capable

of restricting the half opening angle from X-ray (θ_{tor}), but it can restrict the mid-IR half opening angle (σ). This issue is solved when both viewing and opening angles are linked (bS2 baseline model). We found that all the parameters can be constrained in bS2 baseline model using $\theta_{tor} = 90 - \sigma$. The link between half opening angles suggests a common origin for both emissions. Indeed, the statistic does not improve if these two parameters are allowed to vary individually. Therefore, the

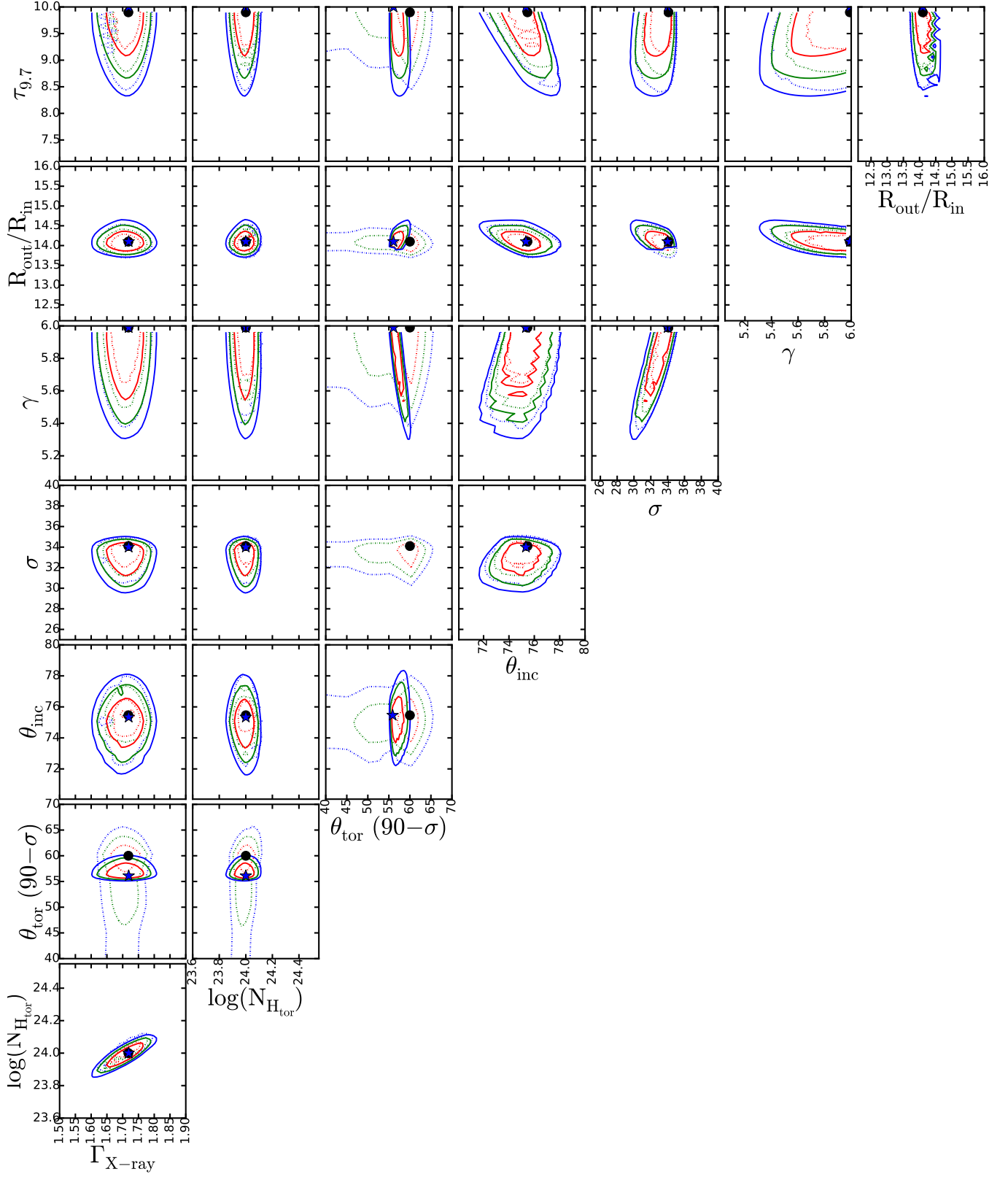


Figure 6. Two-dimensional $\Delta\chi^2$ contours for the resulting free parameters when we used the bS1 (dotted lines) and the bS2 (solid lines) baseline models to fit IC 5063. The red, green and blue (dotted and solid) lines show the contours at 1σ , 2σ , and 3σ , respectively. The black circles and blue stars are the resulting values for each parameter using the bS1 and bS2 baseline models, respectively. Notice that these values are reported in Columns 2 and 4 of Table 1.

bS2 baseline model, where the viewing and half-opening angles are tied together, is enough to explain the observations at both wavelengths. The fact that the inclination and half-opening angles from mid-IR and X-ray are directly linked to the same value is consistent with previous results (Farrah et al. 2016). Furthermore, the σ parameter could be related to the opening angle of the ionization cone, which is a tracer of [OIII] emission (e.g. García-Bernete et al. 2019). Schmitt et al. (2003) presented the observation in the [OIII] filter from *Hubble Space Telescope* of IC 5063. They found that this emission is extended and aligned with the radio emission and the host galaxy major axis. These results are similar to those found by Morganti et al. (1998). According to Schmitt et al. (2003) the [OIII] emission can be represented by a bicone centered at the nucleus, with an opening angle of $\alpha(\text{cone}) = 60^\circ$, extending for ~ 2.6 kpc along P.A. = -65° and ~ 660 pc along the perpendicular direction. Using this measurement of the ionization opening angle, we obtained a free of cone half opening angle of $\alpha(\text{cone} - \text{free}) \sim 60^\circ$ ¹⁰. This suggests the torus occupies a free of cone area although it does not fill it up completely.

The borus02 model is capable of separating the density of the reprocessed material and that of the LOS. This option allows us to explore if the material that produces the reflection component is different from that producing the obscuration along the LOS (see also Baloković et al. 2018). We tested the scenario in which both N_H are linked. We found that $\Delta\chi^2$ increases ($\chi^2/\text{d.o.f} = 706.15/649$) if we fit the IC 5063 spectra using the bS2 baseline model and we assume that $N_{H_{\text{los}}} = N_{H_{\text{tor}}}$ (best fit result in $\log(N_H) = 23.25 \pm 0.02$). We compared this $\chi^2/\text{d.o.f}$ with bS2 statistic through f-test and we obtained a low probability value of 1.91×10^{-6} for the null hypothesis. Therefore, a scenario where these two values are different is statistically preferred. In Figure 7 (left), we show the two dimensional χ^2 distributions for $N_{H_{\text{los}}}$ versus $N_{H_{\text{tor}}}$ parameters when we used the bS2 baseline model. We found that these parameters are not the same at 3σ level. Therefore, $N_{H_{\text{tor}}}$ is larger than the $N_{H_{\text{los}}}$ beyond parameter degeneracy (see also Table 1). Note that in a scenario where both parameters belong to the same structure it is not feasible that $N_{H_{\text{tor}}}$ is larger than $N_{H_{\text{los}}}$, as it is our case (see Table 1), because the former is the average density and the latter decreases with the azimuthal angle. Therefore, $N_{H_{\text{los}}}$ and $N_{H_{\text{tor}}}$ parameters measure the N_H of different absorbing materials. This result is

also found by Baloković et al. (2018). As a final caveat on the subject, we found that $N_{H_{\text{los}}}$, $N_{H_{\text{tor}}}$, and Γ parameter are partially degenerated. We think that this coupling between parameters is due to the natural degeneracy between obscuration and power-law steepness, where high $N_{H_{\text{los}}}$ and low Γ could mimic, at a certain level, to low $N_{H_{\text{los}}}$ and high Γ (see Figures 7 and 6).

Another way to explore the properties of the torus taking into account the information at both wavelength ranges is through the column density and the optical depth from X-ray and mid-IR models, respectively. The two parameters are associated with the density of the obscuring material. The link between these parameters is not straightforward because the $N_{H_{\text{tor}}}$ is an average measurement of the column density at the inner parts of the torus (where the reflection is produced), while the $\tau_{9.7}$ is a measurement of the equatorial optical depth. We considered the relationship between extinction and column density, assuming a constant dust-to-gas ratio and the relation between the optical depth at $9.7 \mu\text{m}$ and that in V band (Nenkova et al. 2008b; Feltre et al. 2012)¹¹. Following these considerations and using the values reported in Table 1 for the bS2 baseline model, we obtained a column density of $\log(N_{H_{\tau_{9.7}}}) > 23.65 \text{ cm}^{-2}$ in the equatorial plane. This value is already consistent with $N_{H_{\text{tor}}}$. However, strictly speaking, to compare it with $N_{H_{\text{tor}}}$, we must calculate the average column density using the dependence of the density distribution with the azimuthal angle. Nevertheless, the resulting upper limit will always be less restrictive than the $N_{H_{\tau_{9.7}}}$ reported above. On the other hand, we also compare the expected LOS column density from the dust distribution with the actual calculated the LOS column density $N_{H_{\text{los}}}$ considering the inclination angle and the dust density distribution values from the bS2 baseline model¹². The resulting value is $\log(N_{H_{\tau_{9.7}}}^{\text{los}}) > 23.03$, which is consistent with the $N_{H_{\text{los}}}$ value.

Therefore, we were able to find evidence suggesting that the structure that produces the continuum (mid-IR) and the reprocessed (X-ray) emissions is the same. This suggests that the reflection component has its origin in the AGN torus. Indeed, the smooth and the borus02 models individually fitting the mid-IR and X-ray spectra (individual fits reported in Table 2), also show consistent viewing angles and width of the torus,

¹¹ $\tau_{9.7} = 0.042 * \tau_\nu$

¹² We used the following equation to calculate the N_H in the sight of line derived from the mid-IR optical depth: $N_{H_{\tau_{9.7}}}^{\text{inc}} (\text{cm}^{-2}) = \frac{1.086}{0.042} * \tau_{9.7} * 1.9 \times 10^{21} * e^{-\gamma \cos(\theta_{\text{inc}})}$. This equation consider the density function (see equation 3 in Fritz et al. 2006), which depend on θ_{inc} and γ .

¹⁰ $\alpha(\text{cone} - \text{free}) = \frac{180^\circ - \alpha(\text{cone})}{2}$

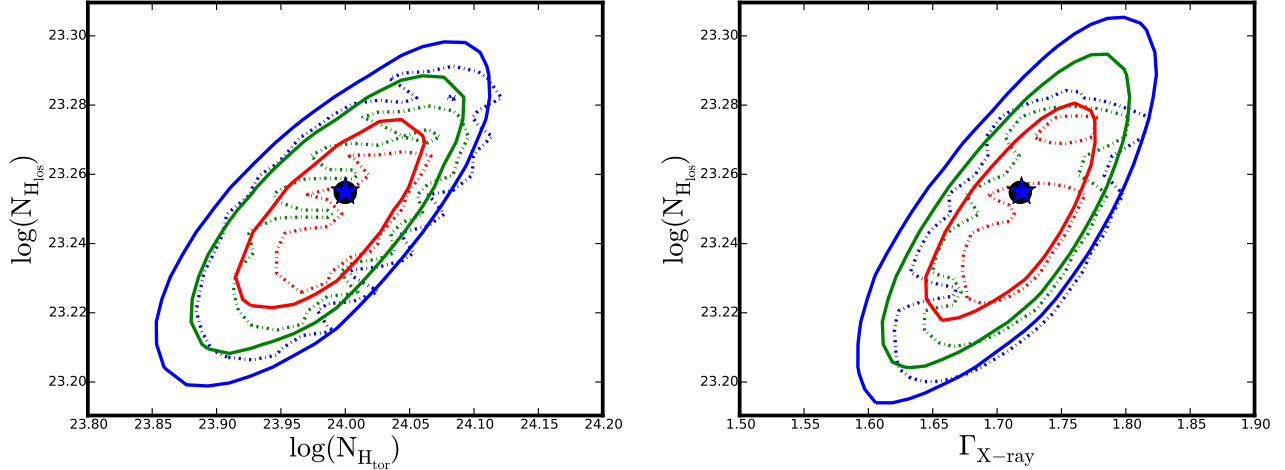


Figure 7. Two dimensional $\Delta\chi^2$ contours for the LOS, density profile, and the torus $N_{H_{tor}}$ for bs (dotted lines) and bs2 (solid lines) baseline models. The red, green, and blue lines are 1, 2, and 3 σ contours. The values reported in table 1 are shown with a black circle and blue star for bs and bs2 baseline models, respectively.

although the θ_{tor} and θ_{inc} parameters are better restricted when using the bs2 baseline model. This result has been largely argued in literature although we lacked of observational evidence. Although without simultaneous fitting, Farrah et al. (2016) also look for the similarities on the geometrical distribution resulting from the mid-infrared and X-ray spectroscopic analysis of the radio galaxy IRAS 09104+4109. They concluded that both obscurers are consistent with being co-aligned, although viewing angle needed to be fixed to that obtained at mid-infrared wavelengths. Bianchi & Guainazzi (2007) suggested that the widespread presence of a Compton reflection component strongly favors a scenario where most of the FeK α emission comes from the torus and Bianchi et al. (2012) listed reasons why these two components come from a region smaller than 100 pc, associating it to the AGN. One of the strongest arguments in favour of an origin of the reflection component on the torus comes from the FeK α emission line, always attached to the Compton-hump. Iwasawa & Taniguchi (1993) reported for the first time an anti-correlation between the strength of the neutral narrow core of the FeK α emission line and the 2-10 keV luminosity (the so-called “X-ray Baldwin effect” or “Iwasawa-Taniguchi” effect¹³). Page et al. (2004) have also explored this effect and suggested that a possible explanation is a decrease in the C_f of the Compton thick torus when the luminosity increases (see also Boorman et al. 2018). The current work shows one of the first direct

¹³ The baldwin effect is an anti-correlation between the equivalent width and the luminosity found in optical/UV lines.

Parameter	Value
Γ	$1.73 \pm_{0.07}^{0.01}$
$\log(N_{H_{tor}})$	$24.00 \pm_{0.04}^{0.04}$
$\log(N_{H_{los}})$	$23.25 \pm_{0.01}^{0.03}$
θ_{tor}	$59.9 \pm_{15.4}^{2.5}$
θ_{inc}	$75.5 \pm_{2.1}^{2.6}$
$\chi^2/\text{d.o.f.}$	530/464
$i_{F06}(90. - \theta_{inc})$	$14.9 \pm_{0.4}^{0.4}$
σ	$34.2 \pm_{2.2}^{2.5}$
β	0.0
Y	$14.1 \pm_{0.3}^{0.3}$
$\tau_{9.7}$	> 8.9
γ	> 5.6
$\chi^2/\text{d.o.f.}$	148/181

Table 2. The best-fit physical parameters using the borus02 (top) and the smooth (bottom) models for IC 5063.

evidences of the link between the reflection component and the torus.

6.2. Parameters and derived quantities of the dusty structure

The dust torus parameters of IC 5063 have been explored using the Clumpy model and a Bayesian approach on high-resolution spectra and/or photometry by Ramos-Almeida et al. (2011); Alonso-Herrero et al. (2011). The values obtained using our bC1 baseline model, except for θ_{inc} and q do not agree with theirs.

However, it should also be noted that the statistic obtained for this baseline model is not the best for this source. If we compare their values with the ones from our best baseline model (i.e. bS2) we find the Y and θ_{inc} are in well agreement with their error ranges. Meanwhile, our σ value is half of their reported value. Indeed, the smooth model accounts for the same dust in a smaller volume compared to the clumpy models (see also González-Martín et al. 2019a,b). As suggested in the literature, the resulting model parameters and derived quantities seem to strongly depend on the model used, wavelength and/or kind of data (i.e. spectroscopy or photometry). While they mostly rely on near- and mid-IR photometry (with ground-based Q-band spectroscopy), we use spectroscopic data covering mid-IR and X-ray.

On the other hand, Baloković et al. (2018) fitted the *NuSTAR* spectra of IC 5063 using borus02 model. Their values of $\Gamma = 1.75$, $\log(N_{H_{tor}}) = 23.3$, $\log(N_{H_{los}}) = 23.9$, and $\theta_{inc} > 52^\circ$ are consistent with our values within 1σ for the individual fits (see Table 2) and those obtained for the bS2 baseline models (see Table 1). The largest discrepancy is found for the θ_{tor} parameter. Baloković et al. (2018) found $\theta_{tor} < 40^\circ$ which is consistent with the reported value using the individual fit and the bS1 baseline model (see Tables 2 and 1) at the 3σ (see Figure 6). However, this value is not consistent with that obtained by the bS2 baseline model. Note that these values are obtained assuming fix $N_{H_{tor}}$. This might explain the discrepancy found and shows the difficulties to restrict the θ_{tor} using X-ray data alone, reinforcing the need to produce a consistent picture using multiwavelength information.

This issue is also visible in the derived quantities. In the last row of Table 1 we report the dust masses obtained from the mid-IR parameters, which cover a range $0.06 - 30.3 \times 10^5 M_\odot$. Therefore, the dust mass depends on the chosen baseline model to fit the spectra. Despite this, the values are consistent with the ranges reported in other works (Mor et al. 2009; Fritz et al. 2006). Furthermore, Cf is strongly dependent on the baseline model used. Ramos-Almeida et al. (2011) compared the properties of a large sample of Sy1 and Sy2 Seyfert tori using the clumpy torus models. They found that the dusty torus in Sy2 is wider than in Sy1, and is composed of a larger number of clouds with lower optical depth. Our mid-IR covering factors (Cf_{midIR} in Table 1) are consistent with their results (see also Brightman 2015).

We also calculated the R_{out} for each of our baseline models. We find $R_{out} > 23.9$ pc (diameter $\sim 0.2''$) and $R_{out} = 3.4$ pc (diameter $\sim 0.03''$) when using the bC1

and bS2 baseline models to fit the spectra, respectively. This last R_{out} value is consistent with the reported by Ichikawa & Inayoshi (2017) for IC 5063. Therefore, the selection of the baseline model is crucial to obtain meaningful results for both structural parameters and derived quantities. Additionally, note that only the R_{out} obtained using the bC1 baseline model could be detectable at the best spatial resolution provided by ALMA¹⁴. However, ALMA data is also sensitive to the radio jet emission, so a proper study of the SED is required to use ALMA data to study the AGN dust (Pasetto et al. 2019). Finally, we suggest for future works to test as many models as possible with multi-wavelength spectroscopy to try to disentangle which models better reproduces the data before drawing any conclusion on the parameters.

Overall, according to the values of parameters results using the bS2 baseline model, the IC 5063 torus is compact ($R_{out} \sim 3.4$ pc) and relatively thin ($\sigma \sim 34$) structure. Our bS2 baseline model solution also favors a dust torus in which the density profile only has an azimuthal dependence ($\gamma > 5.6$), i.e. a strong decrease on the dust/gas density when the half-opening angle increases.

6.3. About our simultaneous fitting technique

Apart from simultaneously explaining both mid-IR and X-ray continuum emission, the main advantage of being able to link some parameters from mid-IR and X-ray models is that we can find all of them from the final fit (see Fig. 6). Therefore, we can obtain more information and explore the source of obscuration at both wavelengths.

In the case of IC 5063, we found that the best option to fit its spectra is using a combination of the Smooth and borus02 models (bS2). A caveat on this result is that these two models may have been our best choice to fit the data due to their geometric similarities. Indeed, both models assume a smooth distribution arranged in a torus-like structure. Nevertheless, these models assume a different density distribution; the borus02 model assumes a uniform density profile for the gas distribution and the smooth model considers that it decreases towards large azimuths and radii. Additionally, the smooth model assumes that a dusty structure is located between an inner and outer radius while gas can reach the accretion disc. Recently, Tanimoto et al. (2019) constructed the XCLUMPY model that is the radiative transfer of neutral gas at X-rays using the same distribution as the clumpy torus at mid-IR. A combination

¹⁴ The highest spatial resolution obtained with ALMA uses a configuration C43-10 in band 7

of XCLUMPY and Clumpy models might also get good results. We can discard this scenario for IC 5063 since the residuals seen at mid-IR for the Clumpy model are significantly larger than those reported for the smooth mode. However, as we expect different AGN to be better reproduced with different models, we will explore this possibility using a AGN sample in a forthcoming paper (Esparza-Arredondo in preparation).

Finally, a few words on the applicability of this technique to AGN samples. Our technique of simultaneous fitting can be applied to any type of AGN that is not dominated by the host galaxy. The best results could be found when using the high-spatial resolution mid-IR spectra and hard ($> 10\text{keV}$) X-ray spectra to ensure a proper decontamination of the host galaxy and a characterization of the reflection component, respectively. The reflection dominated spectra at X-ray (i.e. with high obscuration towards the LOS) are also better targets. *Spitzer*/IRS spectra can be used as long as the AGN dominates the emission, future *JWST* observations would be needed otherwise.

7. CONCLUSIONS

In this work, we explored if the X-ray reflection component and the mid-IR continuum of AGN are linked to the same structure, i.e. the so-called AGN torus. Showing that is the case, we also investigate if the combination of X-ray and mid-IR spectra and different torus models could help us to restrict the torus physical parameters of the nearby Seyfert IC 5063 galaxy. We considered *Spitzer*/IRS and *NuSTAR* spectra for this analysis. We combined the radiative transfer code *borus02* at X-ray (Baloković et al. 2018) to describe the X-ray reflection and Smooth (Fritz et al. 2006), Clumpy (Nenkova et al. 2008b), or CAT3D-wind (Hönig & Kishimoto 2017) models to describe mid-IR AGN dust to create a set of baseline models. We found that the combination of the *borus02* and Smooth models is the best choice to fit the spectra from both wavelengths of IC 5063.

Moreover, all the parameters of the dusty torus can be constrained if the X-ray and mid-IR inclination and half-opening angles are linked to the same value (bS2 baseline model). This link between parameters suggests that the same structure producing the reflection component is emitting through dust heating at mid-IR. This could be the first time such behavior is confirmed by comparing the expected morphology at and obscuring material distributions at both wavelengths. This technique can be used to infer the physical properties of the torus of any AGN that is not dominated by the host galaxy at mid-IR and shows a significant fraction of the reflection component at X-ray.

The authors thank the anonymous referee for careful reading and constructive suggestion that improved the paper. This work made use of data from the *NuSTAR* mission, a project led by CalTech, managed by JPL, and funded by NASA. We thank the *NuSTAR* Operations, Software and Calibration teams for support with the execution and analysis of these observations. This research has made use of the *NuSTAR* Data Analysis Software (*NuSTARDAS*) jointly developed by the ASI Science Data Center (ASDC, Italy) and CalTech. This work is based in part on observations made with the *Spitzer* Space Telescope, which is operated by the Jet Propulsion Laboratory, California Institute of Technology under a contract with NASA. D. E.-A. acknowledges support from a CONACYT scholarship. This research is mainly funded by the UNAM PAPIIT project IA103118 (PI OG-M). MM-P acknowledges support by KASI postdoctoral fellowships. JM acknowledges financial support from the research project AYA2016-76682-C3-1-P (AEI/FEDER, UE) and the State Agency for Research of the Spanish MCIU through the Center of Excellence Severo Ochoa award for the Instituto de Astrofísica de Andalucía (SEV-2017-0709). C.R.-A. acknowledges the Ramón y Cajal Program of the Spanish Ministry of Economy and Competitiveness through project RYC-2014-15779 and the Spanish Plan Nacional de Astronomía y Astrofísica under grant AYA2016-76682-C3-2-P.

REFERENCES

- Alonso-Herrero, A., Ramos Almeida, C., Mason, R., et al. 2011, *ApJ*, 736, 82
- Antonucci, R. 1993, *ARA&A*, 31, 473
- Asmus, D., Hönig, S. F., Gandhi, P., Smette, A., & Duschl, W. J. 2014, *MNRAS*, 439, 1648
- Baloković, M., Brightman, M., Harrison, F. A., et al. 2018, *ApJ*, 854, 42
- Barvainis, R. 1987, *ApJ*, 320, 537
- Bianchi, S., Matt, G., Balestra, I., Guainazzi, M., & Perola, G. C. 2004, *A&A*, 422, 65
- Bianchi, S., & Guainazzi, M. 2007, The Multicolored Landscape of Compact Objects and Their Explosive Origins, 924, 822
- Bianchi, S., Maiolino, R., & Risaliti, G. 2012, *Advances in Astronomy*, 2012, 782030

- Bohlin, R. C., Savage, B. D., & Drake, J. F. 1978, *ApJ*, 224, 132
- Brightman, M., & Nandra, K. 2011, *MNRAS*, 413, 1206
- Brightman, M. 2015, *TORUS2015*
- Boorman, P. G., Gandhi, P., Baloković, M., et al. 2018, *MNRAS*, 477, 3775
- Efstathiou, A., & Rowan-Robinson, M. 1995, *MNRAS*, 273, 649
- Elitzur, M., & Netzer, H. 2016, *MNRAS*, 459, 585
- Fabian, A. C. 1998, *American Institute of Physics Conference Series*, 431, 247
- Farrah, D., Baloković, M., Stern, D., et al. 2016, *ApJ*, 831, 76
- Feltre, A., Hatziminaoglou, E., Fritz, J., & Franceschini, A. 2012, *MNRAS*, 426, 120
- Fritz, J., Franceschini, A., & Hatziminaoglou, E. 2006, *MNRAS*, 366, 767
- Fukazawa, Y., Furui, S., Hayashi, K., et al. 2016, *ApJ*, 821, 15
- Furui, S., Fukazawa, Y., Odaka, H., et al. 2016, *ApJ*, 818, 164
- García-Bernete, I., Ramos Almeida, C., Alonso-Herrero, A., et al. 2019, *MNRAS*, 486, 4917
- Ghisellini, G., Haardt, F., & Matt, G. 1994, *MNRAS*, 267, 743
- González-Martín, O., Masegosa, J., Hernán-Caballero, A., et al. 2017, *arXiv:1704.06739*
- González-Martín, O., Masegosa, J., García-Bernete, I., et al. 2019, *arXiv e-prints*, *arXiv:1908.11381*
- González-Martín, O., Masegosa, J., García-Bernete, I., et al. 2019, *arXiv e-prints*, *arXiv:1908.11389*
- Granato, G. L., & Danese, L. 1994, *MNRAS*, 268, 235
- Harrison, F. A., Craig, W. W., Christensen, F. E., et al. 2013, *ApJ*, 770, 103
- Hatziminaoglou, E., Fritz, J., Franceschini, A., et al. 2008, *MNRAS*, 386, 1252
- Hatziminaoglou, E., Fritz, J., & Jarrett, T. H. 2009, *MNRAS*, 399, 1206
- Hönig, S. F., Kishimoto, M., Gandhi, P., et al. 2010, *A&A*, 515, A23
- Hönig, S. F., & Kishimoto, M. 2010, *A&A*, 523, A27
- Hönig, S. F., & Kishimoto, M. 2017, *ApJL*, 838, L20
- Ichikawa, K., Packham, C., Ramos Almeida, C., et al. 2015, *ApJ*, 803, 57
- Ichikawa, K., & Inayoshi, K. 2017, *ApJL*, 840, L9
- Ikedo, S., Awaki, H., & Terashima, Y. 2009, *ApJ*, 692, 608
- Iwasawa, K., & Taniguchi, Y. 1993, *ApJL*, 413, L15
- Krolik, J. H., Madau, P., & Zycki, P. T. 1994, *ApJL*, 420, L57
- Krolik, J. H., & Begelman, M. C. 1988, *ApJ*, 329, 702
- Koyama, K., Awaki, H., Iwasawa, K., & Ward, M. J. 1992, *ApJL*, 399, L129
- Laor, A. 1991, *ApJ*, 376, 90
- Lebouteiller, V., Barry, D. J., Spoon, H. W. W., et al. 2011, *ApJS*, 196, 8
- Liu, T., & Wang, J.-X. 2010, *ApJ*, 725, 2381
- Liu, Y., & Li, X. 2015, *MNRAS*, 448, L53
- Martínez-Paredes, M., Aretxaga, I., Alonso-Herrero, A., et al. 2017, *MNRAS*, 468, 2
- Matt, G., Perola, G. C., & Piro, L. 1991, *A&A*, 247, 25
- Mor, R., Netzer, H., & Elitzur, M. 2009, *ApJ*, 705, 298
- Morganti, R., Oosterloo, T., & Tsvetanov, Z. 1998, *AJ*, 115, 915
- Morganti, R., Oosterloo, T., Oonk, J. B. R., Frieswijk, W., & Tadhunter, C. 2015, *A&A*, 580, A1
- Murphy, K. D., & Yaqoob, T. 2009, *MNRAS*, 397, 1549
- Nandra, K., & George, I. M. 1994, *MNRAS*, 267, 974
- Nenkova, M., Sirocky, M. M., Ivezić, Ž., & Elitzur, M. 2008, *ApJ*, 685, 147-159
- Nenkova, M., Sirocky, M. M., Nikutta, R., Ivezić, Ž., & Elitzur, M. 2008, *ApJ*, 685, 160-180
- Netzer, H. 2015, *ARA&A*, 53, 365
- Page, K. L., O'Brien, P. T., Reeves, J. N., & Turner, M. J. L. 2004, *MNRAS*, 347, 316
- Panuzzo, P., Rampazzo, R., Bressan, A., et al. 2011, *A&A*, 528, A10
- Pasetto, A., González-Martín, O., Esparza-Arredondo, D., et al. 2019, *ApJ*, 872, 69
- Peeters, E., Spoon, H. W. W., & Tielens, A. G. G. M. 2004, *ApJ*, 613, 986
- Pfeffermann, E., Briel, U. G., Hippmann, H., et al. 1987, *Proc. SPIE*, 733, 519
- Pier, E. A., & Krolik, J. H. 1993, *ApJ*, 418, 673
- Ramos Almeida, C., Levenson, N. A., Rodríguez Espinosa, J. M., et al. 2009, *ApJ*, 702, 1127
- Ramos Almeida, C., Levenson, N. A., Alonso-Herrero, A., et al. 2011, *ApJ*, 731, 92
- Ramos Almeida, C., & Ricci, C. 2017, *Nature Astronomy*, 1, 679
- Ricci, C., Walter, R., Courvoisier, T. J.-L., & Paltani, S. 2011, *A&A*, 532, A102
- Ricci, C., Ueda, Y., Paltani, S., et al. 2014, *MNRAS*, 441, 3622
- Schartmann, M., Meisenheimer, K., Camenzind, M., Wolf, S., & Henning, T. 2005, *A&A*, 437, 861
- Schmitt, H. R., Donley, J. L., Antonucci, R. R. J., et al. 2003, *ApJS*, 148, 327
- Shlosman, I. 2005, *The Evolution of Starbursts*, 783, 223
- Shu, X. W., Yaqoob, T., & Wang, J. X. 2010, *ApJS*, 187, 581

- Siebenmorgen, R., Heymann, F., & Efstathiou, A. 2015, *A&A*, 583, A120
- Stalevski, M., Fritz, J., Baes, M., Nakos, T., & Popović, L. Č. 2012, *MNRAS*, 420, 2756
- Tacconi, L. J., Genzel, R., Blietz, M., et al. 1994, *ApJL*, 426, 77
- Tanaka, Y., Inoue, H., & Holt, S. S. 1994, *PASJ*, 46, L37
- Tanimoto, A., Ueda, Y., Odaka, H., et al. 2019, *arXiv:1904.08945*
- Vignali, C., Comastri, A., Cappi, M., & Palumbo, G. G. C. 1997, *Mem. Soc. Astron. Italiana*, 68, 139
- Yang, Q.-X., Xie, F.-G., Yuan, F., et al. 2015, *MNRAS*, 447, 1692
- Urry, C. M., & Padovani, P. 1995, *PASP*, 107, 803